GeoHazards

MDPI

Article

Mass Movements in Wetlands: An Analysis of a Typical Amazon Delta-Estuary Environment

Aline M. Meiguins de Lima [1,*], Vitor Gabriel Queiroz do Nascimento [2], Saulo Siqueira Martins [3], Arthur Cesar Souza de Oliveira [2] and Yuri Antonio da Silva Rocha [4]

[1] Institute of Geosciences, Federal University of Pará, Belém 66075-110, State of Pará, Brazil
[2] Faculty of Geology, Federal University of Pará, Belém 66075-110, State of Pará, Brazil; vitor.vgqn@gmail.com (V.G.Q.d.N.); arthurcsoliveira174@gmail.com (A.C.S.d.O.)
[3] Postgraduate Program in Geophysics, Federal University of Pará, Belém 66075-110, State of Pará, Brazil; ssmsaulo@gmail.com
[4] Postgraduate Program in Environmental Sciences, Federal University of Pará, Belém 66075-110, State of Pará, Brazil; eng.yurirocha@gmail.com
* Correspondence: ameiguins@ufpa.br

Abstract

This study aims to investigate the processes associated with mass movements and their relationship with the behavior of the Amazon River delta-estuary (ADE) wetlands. The methodological approach involves using water spectral indices and ground-penetrating radar (GPR) to diagnose areas of soil water saturation and characterize regions affected by mass movements in Amazonian cities. It also involves identifying areas of critical saturation content and consequent mass movements. Analysis of risk and land use data revealed that the affected areas coincide with zones of high susceptibility to mass movements induced by water. The results showed the following: the accumulated annual precipitation ranged from 70.07 ± 55.35 mm·month^{-1} to 413.34 ± 127.51 mm·month^{-1}; the response similarity across different sensors obtained an accuracy greater than 90% for NDWI, MNDWI, and AWEI for the same targets; and a landfill layer with a thickness variation between 1 and 2 m defined the mass movement concentration in Abaetetuba city. The interaction between infiltration, water saturation, and human-induced land alteration suggests that these areas act as wetlands with unstable dynamics. The analysis methodology developed for this study aimed to address this scenario by systematically mapping areas with mass movement potential and high-water saturation. Due to the absence of geological and geotechnical data, remote sensing was employed as an alternative, and in situ ground-penetrating radar (GPR) evaluation was suggested as a means of investigating the causes of a previously observed movement.

Keywords: Amazonian cities; spectral indices; ground-penetrating radar

check for updates

Academic Editor: Hans-Balder Havenith

Received: 10 June 2025
Revised: 21 July 2025
Accepted: 23 July 2025
Published: 29 July 2025

Citation: de Lima, A.M.M.; do Nascimento, V.G.Q.; Martins, S.S.; de Oliveira, A.C.S.; da Silva Rocha, Y.A. Mass Movements in Wetlands: An Analysis of a Typical Amazon Delta-Estuary Environment. *GeoHazards* **2025**, *6*, 40. https://doi.org/10.3390/geohazards6030040

Copyright: © 2025 by the authors. Licensee MDPI, Basel, Switzerland. This article is an open access article distributed under the terms and conditions of the Creative Commons Attribution (CC BY) license (https://creativecommons.org/licenses/by/4.0/).

1. Introduction

The growth of cities results in various processes of landscape alteration, including physical changes and changes to associated ecosystems. The most influential factors in the physical environment (related to underlying geologic composition, geomorphic processes, sediment dynamics, and climate) control the river environment, with hydrological behavior and soil loss being the main considerations. These factors directly impact on the environmental services that can be generated, such as the maintenance of habitats linked to local fauna and flora. Over the years these factors have become commonplace

in Amazonian cities, where urbanization along riverbanks has led to the modification of floodplains and the creation of an impermeable environment characterized by the intense removal of vegetation [1,2].

The direct consequence is observed in both surface and groundwater recharge areas, as well as in their quality patterns, in addition to the advancement of erosive processes characterized by the presence of mass movements [3]. The shape of the Amazon River delta-estuary (ADE) is determined by shifting alluvial sediments. This configuration depends on the characteristics of the soil profile, runoff, river discharge, and landscape conditions. The displacement of soil masses is related to the soft, marginal slopes of rivers within broad floodplains. In these areas, there is high connectivity between thick soil coverage resulting from weathering and surface/subsurface processes [4].

Historically this development has consolidated, forming a belt of marginal cities along the rivers of the ADE. Their relationship with climatic seasonality and the consequent variation in water behavior (flow and level) is not harmonious as problems related to floods and inundations, or the effects of droughts, are reported annually. Several occurrences have been reported only in the last two decades [5]. Flood extremes marked the years 2009, 2012–2015, 2017, 2019, and 2021–2022, with peaks in 2009, 2012, 2021, and 2022, and minimums in 2010 and 2023 [6,7]. The chronology reveals a very high proximity between extremes, highlighting the need to expand studies on future scenarios associated with climate change and existing social and economic vulnerabilities.

The succession of hazard events demonstrates that risk management is an essential tool for identifying the extent of the affected area, assessing forms of reduction, mitigation, and prevention, aiming to minimize the vulnerability or exposure of the affected population. In the case of mass movements, using geotechnologies through the configuration of Geographic Information Systems (GIS) and coupled statistical methods helps cover large areas and better structure actions for intervention in the affected region [8,9].

The strongest barrier to assessing vulnerabilities is the degree of urbanization. This varies from the central region to the periphery, where there are heterogeneous housing patterns and numerous residents. The cities of the ADE date back to the 17th and 18th centuries [10] and underwent an urban consolidation process that did not prioritize a sustainable relationship with the waters, with the predominance of landfills and channeling practices as well as the intense removal of marginal vegetation cover.

These activities contributed to the modification of the floodplain. The first cities founded were Belém, Gurupá, Cametá, Vigia, and Salvaterra, totaling nine cities in the ADE between 1700 and 1800, with the emergence of Ponta de Pedras, Barcarena, Santana, and Oeiras do Pará [10]. The location prioritized strategic points aimed at promoting defense, trade, state representation, and religious centers [11]. Thus, problems during flood seasons and the emergence of erosive processes became elements of adaptation for these populations as environmental issues were not a priority at the time of the cities' founding and growth.

The growth of the Metropolitan Region of Belém (MRB) went through several phases of expansion until reaching its current configuration. Initially formed by the municipalities of Belém, Ananindeua, Marituba, Benevides, and Santa Bárbara do Pará (1995), it was later expanded with the inclusion of Santa Isabel do Pará (2010), Castanhal (2011), and finally Barcarena in 2023 [12]. The environmental relationship of this urban expansion demonstrates a reduction in the representation of forested areas and rivers, indicating that these environments are perceived primarily as resource sources rather than being valued for their functional significance or the provision of environmental services [12].

The cities within the ADE have become vulnerable as they expand into the marginal areas along rivers. This problem becomes more pronounced as the degree of exposure

increases. The imposition on the floodplain site has created a variety of urban contexts built either on land or over water, with extensive areas developed according to the typology of human settlements known as "*baixada*" (lowland areas), translated as precarious urban settlements or social housing [13].

This scenario reinforces the need for improved governance and a deeper understanding of the natural processes involved. It is also essential to implement appropriate mitigation actions to protect populations at risk and to monitor the environmental risk conditioning processes evaluated [14].

In this context, the ADE is framed as the object of investigation, represented by the coastal strip adjacent to the estuary where an extensive floodplain area is vulnerable to erosive processes and has a high degree of exposure to soil movement [3]. The runoff process, which is linked to rainfall and variations in water levels, carries soil particles towards the drainage system and favors the occurrence of mass movements in the ADE. The chosen area of study comprises watersheds that drain into the ADE on the right bank of the estuary. In these areas, soil stability is essential for controlling the risk environment in urban areas, which tend to exhibit high erosion rates and sediment transport under the influence of the ADE.

The proposed objective is to investigate the processes associated with mass movements and their relationship with the behavior of the Amazon River delta-estuary wetlands. The methodological approach is based on diagnosing the area, analyzing it using spectral water indices, and characterizing areas affected by mass movements using ground-penetrating radar (GPR). As a result, the most critical areas associated with soil water saturation were zoned.

2. Materials and Methods

2.1. Study Area

The Amazon River delta-estuary (ADE) [15,16] is represented by the municipalities located within a radius of up to 5 km from the Amazon River, including the cities of Barcarena and Abaetetuba in the state of Pará. These are urban centers developed in river deltas which are vulnerable to variation in water levels, situated at altimetric levels at sea level or low elevations, prone to the effects of water level variations, and densely populated with many infrastructure deficiencies. Their inhabitants face the effects of water, soil, and air pollution in addition to precarious housing infrastructure [17].

The geological context is characterized by a cover of detrital and siliciclastic sediments, which are associated with a variability in morphology resulting from the distribution of muddy versus sandy levels [15]. The area of coverage is defined by the boundaries of the watersheds that flow into the delta-estuary due to the object of analysis being the occupation of marginal areas along watercourses (Figure 1A). It is bordered by the municipalities of Barcarena and Abaetetuba (Figure 1B) and forms part of the delta-estuary of the Amazon River in northern Brazil (Figure 1C).

2.2. Research Design

The adopted sequence starts with the diagnosis of the area through the configuration of the base cartography, the characterization of the area affected by mass movements using ground-penetrating radar (GPR), and the identification of the most critical areas associated with soil water saturation. Figure 2 summarizes the main steps, highlighting the following methodological elements:

(1) Configuration of the applied information system and the supporting cartography;
(2) Adjustment of geospatial relationships associated with the scale and spatial resolution of the sensors adopted;

(3) Evaluation of the following main analysis products:

(a) Precipitation—for characterizing the region's rainfall regime;

(b) Definition of the regional pattern, with the description of physical aspects associated with elevation, drainage network, groundwater, and relief units;

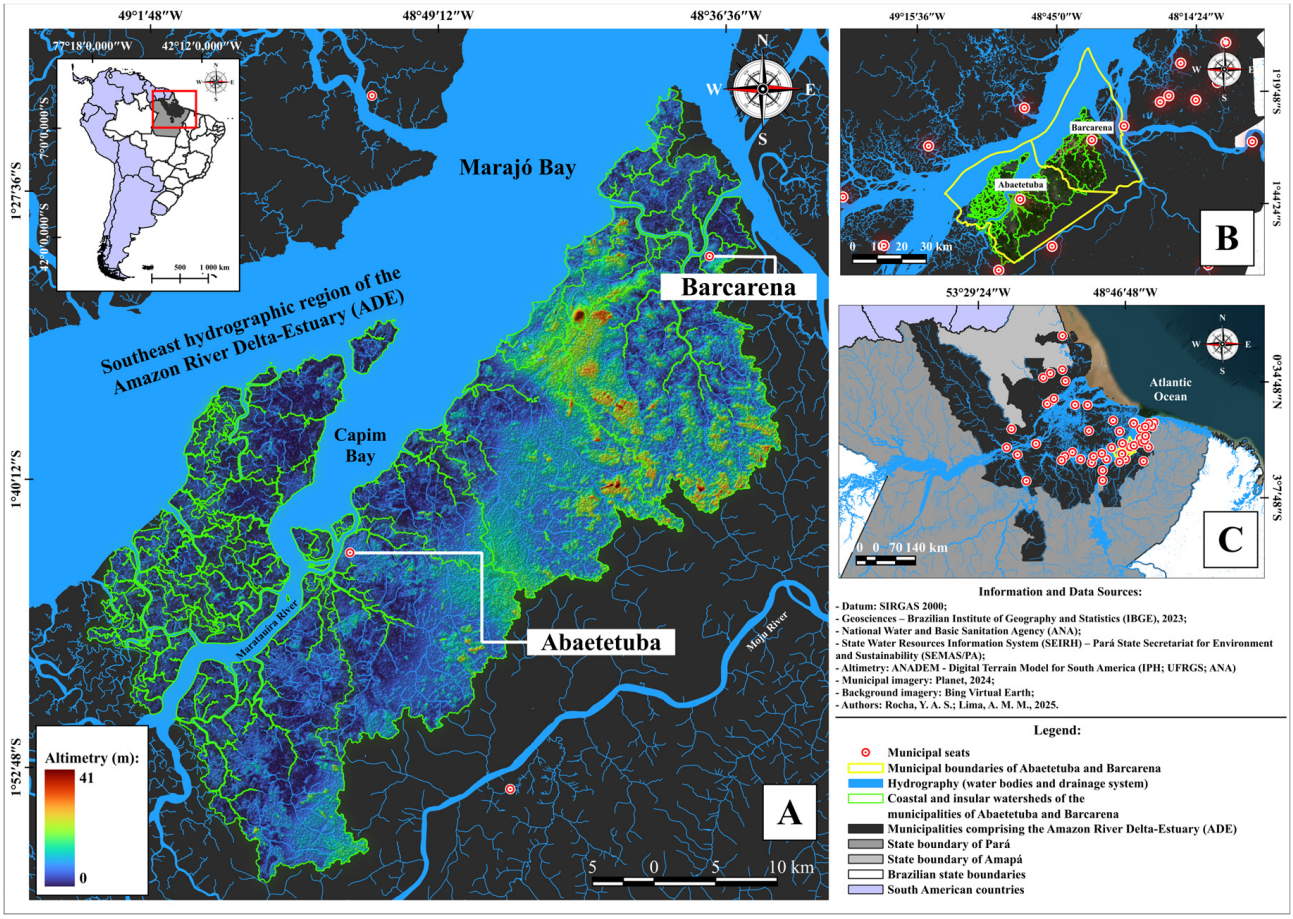


Figure 1. Amazon River delta-estuary (ADE): coastal and island river basins of the municipalities of Abaetetuba and Barcarena. (**A**) Elevation and drainage system. (**B**) Municipal boundaries. (**C**) Location in the delta-estuary of the Amazon River.

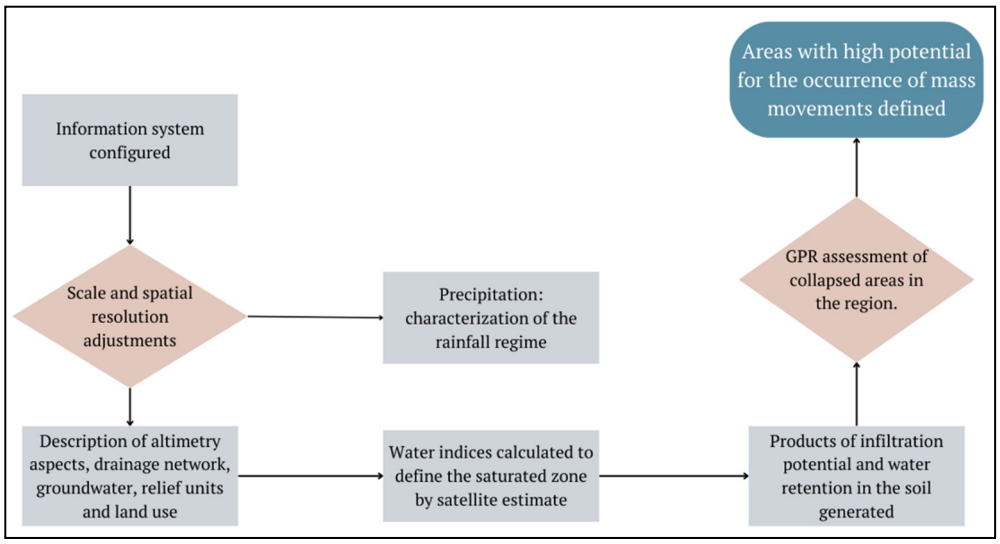


Figure 2. Survey workflow developed.

(4) Application of water indices for characterizing the saturated zone through satellite estimation, as well as evaluation products for the potential of water infiltration and retention in the soil, derived from surface runoff behavior and soil textural characteristics;
(5) Zoning according to areas with the highest potential for mass movements due to soil saturation characteristics and land use;
(6) In situ evaluation using Ground-Penetrating Radar (GPR) of areas that experienced collapse and their relationship with the obtained zoning.

The theoretical approach considers that deltaic systems are exposed to multiple vulnerability scenarios in different social, economic, and environmental contexts, which are determined as a result of exposure, stress, and susceptibility [1]. The susceptibility to mass movements is determined by considering the interplay between the scars on the ground that evidence movement and the impacts of the factors that induce instability [9]. The risk evaluation represents the product of the hazard event probability and the socio-environmental vulnerabilities associated with it, where the exposure degree and the hazard frequency are relevant points that define the risk intensity [8]. The vulnerability of populations in river deltas depends on physical and socioeconomic factors, such as where people live in relation to water levels [17]. This approach is important for modeling hazard zones and validating risk maps, which are used to predict the potential consequences of disasters and help to plan for their impact.

2.3. Diagnosis and Assessment

In the assessment of the region, geological and geomorphological characteristics, altimetry, surface and groundwater conditions, rainfall, and infiltration potential in the saturated zone were evaluated. Tables 1 and 2 summarize the information bases used and extracted from Google Earth Engine (GEE), which were then validated by the cited authors (see the 'Source' column). The tables also show the parameters calculated for the definition of spectral indices [18,19].

Table 1. Assumed information base and associated sensors. Grace (PG), the normalized difference water index (NDWI), the modified normalized difference water index (MNDWI), the water ratio index (WRI), and the automated water extraction index (AWEI).

Description	Source	Indicator
MODIS Ground, bands 1–7, 500 m resolution.	[20]	MNDWI, WRI, and AWEI
MODIS Ground, water content response, 500 m resolution.	[20]	NDWI
GRACE, water mass equivalent (water thickness) anomalies, derived from time-varying gravity observations, 111 km resolution.	[21]	PG
Shuttle Radar Topography Mission. The SRTM V3 (SRTM Plus) product is provided by NASA JPL at 1 arcsecond (~30 m) resolution.	[22]	Digital elevation model and landform
The datasets at 3 arcseconds (~90 m) are the void-filled DEM, hydrologically conditioned DEM, and drainage (flow) direction.	[23]	Hydrographic density
Soil water content (% vol.) for 33 kPa and 1500 kPa suctions predicted at 6 standard depths (200 cm) at 250 m resolution.	[24,25]	Infiltration potential

Table 1. *Cont.*

Description	Source	Indicator
Hansen Global Forest Change v1.11 (2000–2023), 30.92 m resolution. Time-series analysis of Landsat images—global forest extent and change.	[26]	Land cover change
The volume of water stored in the soil and accessible to plants is a parameter used in the modeling of agroclimatic risk in Brazil.	[27,28]	Soil available water

Table 2. Parameters evaluated: the normalized difference water index (NDWI), the modified normalized difference water index (MNDWI), the water ratio index (WRI), and the automated water extraction index (AWEI).

Parameters			Source
$NDWI = (G - NIR)/(G + NIR)$ $MNDWI = (G - SWIR1)/(G + SWIR1)$ $WRI = (G + R)/(NIR + SWIR1)$ $AWEI = B + (2.5 * G) - 1.5 * (NIR + SWIR1) - (0.25 * SWRI2)$			[18,19]
Spectral Range—MODIS Sensor Bands Product MOD09A1			
Band 3	*B*	Blue	459–479 nm
Band 4	*G*	Green	545–565 nm
Band 1	*R*	Red	620–670 nm
Band 2	*IVP*	Near-infrared	841–875 nm
Band 5	*SWIR1*	Shortwave infrared	1230–1250 nm
Band 6	*SWIR2*	Shortwave infrared	1628–1652 nm

2.4. Rainfall Distribution Assessment

In the assessment of rainfall distribution, the following four decadal intervals were compared: 1980–1989 (I1), 1990–1999 (I2), 2000–2009 (I3), and 2010–2019 (I4). The information data available defines a climatology time series, and the decade range is based on this. The data were obtained from the rainfall station 148010 (01°45′01″ S/48°52′01″ W) of the National Water and Basic Sanitation Agency (ANA), made available through the HidroWeb platform [29]. Means, standard deviations, and the normality of the decadal intervals were calculated using the Shapiro–Wilk test. Given the non-normal distribution of the data ($p < 0.05$), the non-parametric Kruskal–Wallis test was applied to determine whether there were statistically significant differences ($p < 0.05$).

2.5. Assessment of Saturated Zone Behavior

The composition of water indices for characterizing the saturated zone adopted the works of Landerer and Swenson [21], Li et al. [30], Laonamsai et al. [31], and Liu et al. [19] as references. April 2021 was used as the baseline month–year as it represents the rainy season in the region and has the lowest cloud cover. These indices detect changes in relative water content, where values ≥ 0 indicate greater presence and the opposite indicates lower water content. NDWI and MNDWI range from -1 to 1, while WRI and AWEI can exceed this range, although maintaining the same behavioral pattern (Table 2).

The use of the GRACE sensor showed a major limitation due to its spatial resolution. However, since it is a product aimed at detecting equivalent water mass anomalies [21], its importance was recognized in strengthening the identification of a zone with greater groundwater contribution.

The definition of water retention potential in the saturated zone (superficial soil layer) used products for soil textural characterization [27] and hydrographic density [23]. These

were weighted on a scale from 1 (lowest water retention potential) to 5 (highest water retention potential); subsequently, the matrix product was reclassified into the categories of very high, high, moderate to high, moderate to low, low, and very low potential. The objective was to define the behavior of water stored in the soil, considering aspects related to texture (grain size); layers with contrasting properties in the soil profile; and groundwater close to the surface. The expected pattern is an increase in sandy texture classes up to medium texture as fine fractions (silt plus clay) increase, reaching the maximum limit in silty texture classes. After that, the general trend is a decrease toward texture classes with a predominance of the clay fraction [28].

In the characterization of wetland areas most favorable for water concentration, an association was adopted between infiltration potential (soil water content (% volume) up to 200 cm) and water retention in the saturated zone, characterizing surface and subsurface retention areas. The use of multiple sensors with different spatial resolutions had its effect reduced by pixel resampling (90 m), aiming for suitability in integrated processing.

The model generated to characterize areas with the highest potential for movement due to water accumulation in the surface soil layers used the product of infiltration potential distribution (where the closer it is to 1, the greater the concentration) and water saturation, based on the soil's textural characteristics. The resulting categorization took into account the increased effect of the degree of intensification of existing land use. This method is based on the principle of the ecological cooling service function of soil cover [32], reflecting the greater water content and slower evaporation in the presence of vegetation (shading effect) and the intense evaporation that occurs in its absence.

In the comparative analysis between the indices, a regular grid of points (1050) distributed across the area was adopted, using the Euclidean distance between them as a reference. The objective was to identify the zones with the highest characterization of water retention in the soil, as well as to evaluate the effect of the resulting dispersion.

2.6. Ground-Penetrating Radar (GPR) Survey

Ground-penetrating radar (GPR) is a high-resolution geophysical method that uses the emission of high-frequency electromagnetic pulses to image dielectric discontinuities in the subsurface [33]. The waves are transmitted by a transmitting antenna and reflected by interfaces where there is a contrast in the dielectric properties of the materials. These reflections are captured by a receiving antenna. The frequency range used in GPR generally varies between 10 MHz and 2.5 GHz. Higher frequencies allow for greater resolution but with shallower investigation depth, while lower frequencies favor deeper penetration at the cost of resolution loss [34].

In the field acquisitions the GSSI SIR-3000 system was used coupled with a 200 MHz monostatic antenna, operating in continuous acquisition mode by distance. This configuration was selected to offer a balance between resolution and depth, suitable for the geological characteristics and the study's objectives. The raw data were processed using the ReflexW software version 1.0, applying conventional preprocessing procedures, including gain correction, background noise removal, frequency filtering, and migration, aiming to enhance the reflections of interest and facilitate the stratigraphic and structural interpretation of the radar profiles.

The data acquisition focused on obtaining twelve radargram sections up to two meters deep in an area affected by mass movements (years 2014 and 2023) in the municipality of Abaetetuba (PA). Between the sections surveyed, seven were conducted along public roads oriented parallel to the coastal line adjacent to the estuary, with a predominant NE–SW direction. The remaining five sections were arranged perpendicularly, following a NW–SE direction. Topographic correction was not applied as the investigated area

presented an almost flat terrain without the significant altimetric variations that would justify this procedure.

3. Results

3.1. Wetland Profile: Influence of Rainfall

Wetland areas are saturated and inundated for periods depending on tidal influence and/or variations in the water level of rivers, which are related to rainfall frequency and intensity. These factors directly affect water-table recharge and other hydrological indicators, such as runoff potential, a driver of soil erosion [35]. Although rainfall behaviors have changed over the last few decades, it continues to significantly impact soil water saturation in addition to the effect of water level variations.

The results showed that rainfall follows a well-defined pattern (monthly average), with a rainy season (P+) (December to May) and a less rainy season (P−) (June to November) over the 40 years studied. The accumulated annual precipitation ranged from 70.07 ± 55.35 mm·month^{-1} to 413.34 ± 127.51 mm·month^{-1}. No statistically significant differences were found between the decadal intervals ($p < 0.05$). There was an increase of 1.76% in rainfall from I2 compared to I1, a 6.30% increase in I3 compared to I2, and a reduction of 2.76% in I4 compared to I3. During the I2 and I3 intervals there was an increase in rainfall in both P+ and P−, ranging from 0.12% to 8.51%, compared to I1 and I2, respectively (Figure 3).

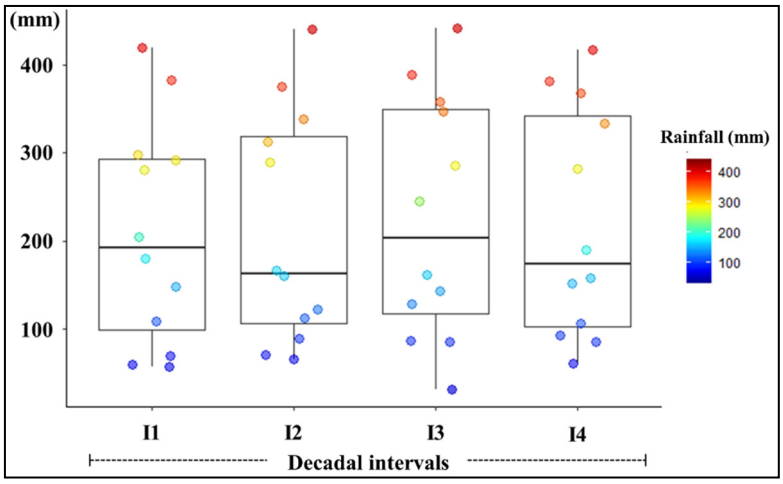


Figure 3. Decadal distribution of precipitation (monthly average): 1980–1989 (I1), 1990–1999 (I2), 2000–2009 (I3), and 2010–2019 (I4).

The intensification of rainfall observed during I3 may be associated with the higher frequency of La Niña events, which promote the cooling of equatorial Pacific waters, reinforcing the Walker circulation and favoring the displacement of the Intertropical Convergence Zone (ITCZ) southward, increasing rainfall in Eastern Amazonia. Meanwhile, in I4, the predominance of El Niño events, characterized by Pacific warming, tends to weaken atmospheric circulation and shift the ITCZ northward, reducing rainfall in the region [35–37].

3.2. Wetland Profile: Geological–Geomorphological Aspects

The region presents the greatest amplitudes in the east-northeast, decreasing towards the riverbanks, with the predominance of low slopes (Figure 4). The classification by landforms indicated gentle amplitudes (Unit 1), usually associated with low-slope hillsides

(less than 2%, Unit 2), with an alternation of well-defined valleys (Unit 3) and more open ones (Unit 4).

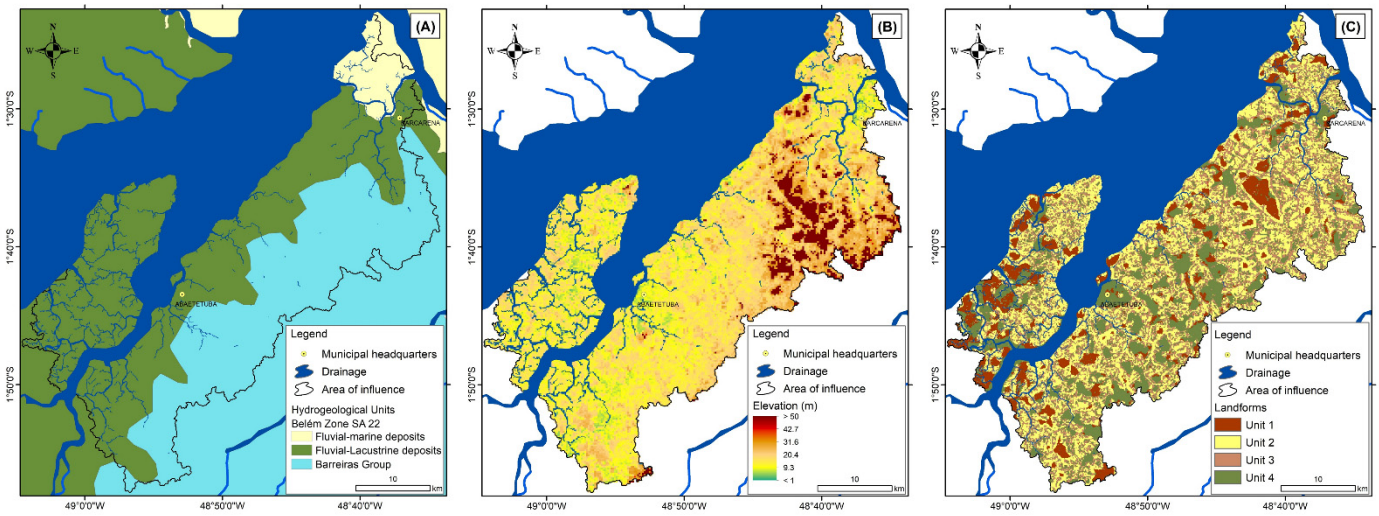


Figure 4. (**A**) Hydrogeological units, (**B**) elevation levels, and (**C**) landforms: geological and geomorphological evaluation.

The marginal areas along the rivers are consistent with fluvial deposits, while the others correspond to the sediments of the Barreiras Group (detrital, siliciclastic sediments, of fluvial and marine origin, ranging from fine to coarse sands, with a predominance of angular grains, reddish-gray clays), which define the "Tabuleiros da Zona Bragantina". The dominant structure is the prevalence of fluvial plains with low relief amplitude (less than 30 m), underlain by sedimentary rocks of Tertiary or Tertiary-Quaternary age from the Barreiras Group and post-Barreiras sediments (sands generally fine to medium, and locally coarse to conglomeratic), frequently covered by detrital-lateritic layers. The dissection forms exhibit rounded reliefs, similar to broad and smooth hills. The landscape also includes the alluvial plain (*várzea*), with meandering river channels, floodplains, and marginal levees, as well as the estuarine plain, featuring estuarine channels and muddy tidal plains. The resulting soil cover consists of well-drained levels with low natural fertility, thick and leached, typically characterized by Dystrophic Yellow Oxisols, Gleysols, Red-Yellow Argisols, and Quartzarenic Neosols [38–40].

3.3. Wetland Profile: Hydrographic Density and Infiltration Potential

Surface runoff (Figure 5A) and infiltration (Figure 5B) show a relationship conditioned by the topography and texture of the soil–rock alteration profile. Where sandy and medium clayey-to-sandy textures predominated, the behavior was favorable to soil percolation and storage in the saturated zone, indicating the highest potentials (values close to 1) for infiltration behavior.

Sandy soils vary in terms of grain size, clay content, and natural processes (e.g., biological activities); they frequently exhibit high hydraulic conductivity, gas permeability, and specific heat capacity, but low field capacity, organic carbon concentration, and cation exchange capacity [41]. In areas dominated by clayey to very clayey profiles, water would have more difficulty percolating through the soil profile, making surface runoff more likely (indicating surface retention and less percolation toward the saturated zone), characterizing a saturation level very close to the surface [42].

The resulting product (Figure 5C) reflects what is expected for the region based on the characteristics of the relief units, with the predominance of fluvial plains (with low relief amplitude), alluvial (*várzea*), and estuarine plains influenced by tides and muddy textures,

indicating good drainage. Forest areas, including riparian zones, play a fundamental role in soil drainage conditions; however, there are limitations due to current land use practices and soil textural and management characteristics [43].

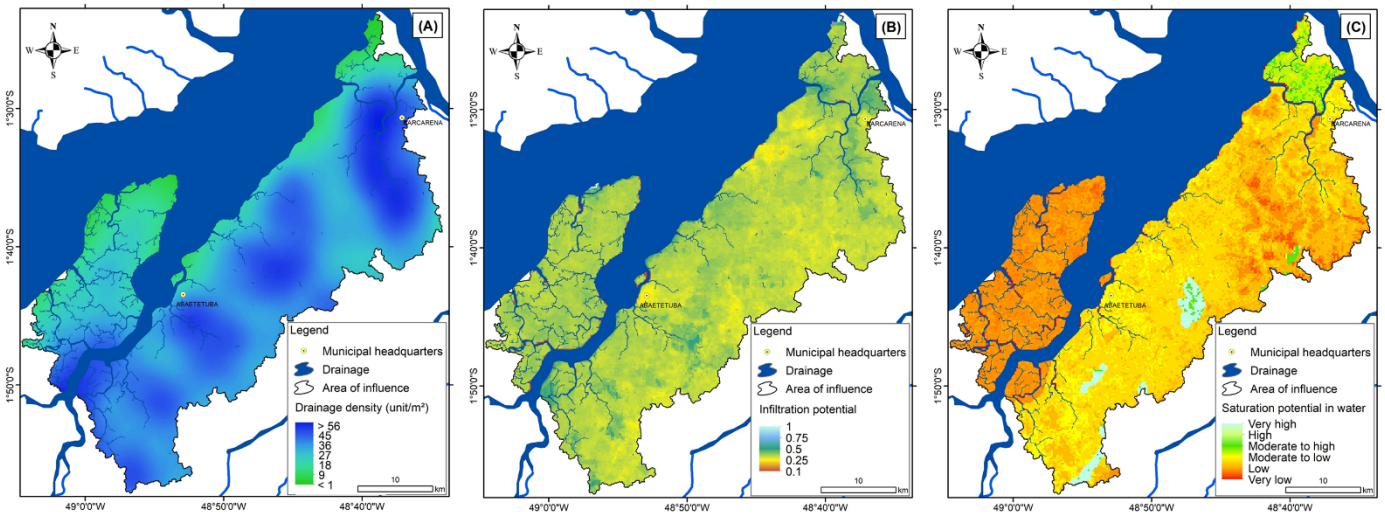


Figure 5. (**A**) Drainage density, (**B**) infiltration potential (up to 200 cm), and (**C**) saturation potential in water: the behavior of water in the soil profile.

3.4. Spectral Indices: Water and Land Cover

The analysis using spectral indices (Table 2) strengthens the observed results, with the concentration of areas with lower response potential being wetlands in the east and southeast in the topographically higher region (Figure 6). The area adjacent to the estuary is the most dynamic, with the spectral indices demonstrating good responsiveness to the presence of water. GRACE showed the greatest limitation, mainly due to its spatial resolution, but it still indicated a strong hydric influence near the surface (Figure 6E).

Spectral indices that include NIR and SWIR bands help enhance the soil/water contrast [44]; however, there are response differences among the water indices. The non-uniformity of response is related to the processes of formation, coverage, and spatial distribution of soil types. These soils exhibit an increase in reflectance from the visible to the near-infrared spectrum, where the 1.4 µm and 1.9 µm bands are related to soil water content, influenced by the types and amounts of minerals, organic matter content, and the surface texture of the soil [45].

Considering values closer to 1 as hydric indicators, NDWI and MNDWI (Figure 6A,B) recorded behaviors similar to that identified for wetlands and vegetated areas [31,46], including WRI (higher values and farther from 0) and AWEI (values ranging from 0 to 1) (Figure 6C,D). The same pattern of response similarity was detected across different sensors, with an accuracy greater than 90% for NDWI, MNDWI, and AWEI for the same targets [47].

The paired analysis of the indices through linear regression obtained $p < 0.0001$ for all compositions and highlighted an R^2 value (0.87) and a Pearson correlation (0.936) for the MNDWI × AWEI relationship, a behavior previously discussed for other regions [31,48]. However, it is important to recognize the extent of landscape alteration (Figure 6F), including urbanization (soil impermeability) and the expansion of exposed soil areas due to the removal of forest cover and its replacement with other forms of land cover, such as those intended for agricultural use.

The comparison with the data from Figure 5, regarding infiltration potential and saturation, and Figure 7A,B shows that the indices concentrate their responses in zones with above 30% infiltration capacity and areas with low to moderately low saturation potential. NDVI was the index that showed the least variation around the mean, while

the other indices displayed similar behavior in terms of mean, median, and standard deviation (Figure 7C), with all 0.75 quartiles approaching values that represent the presence of water (Table 3).

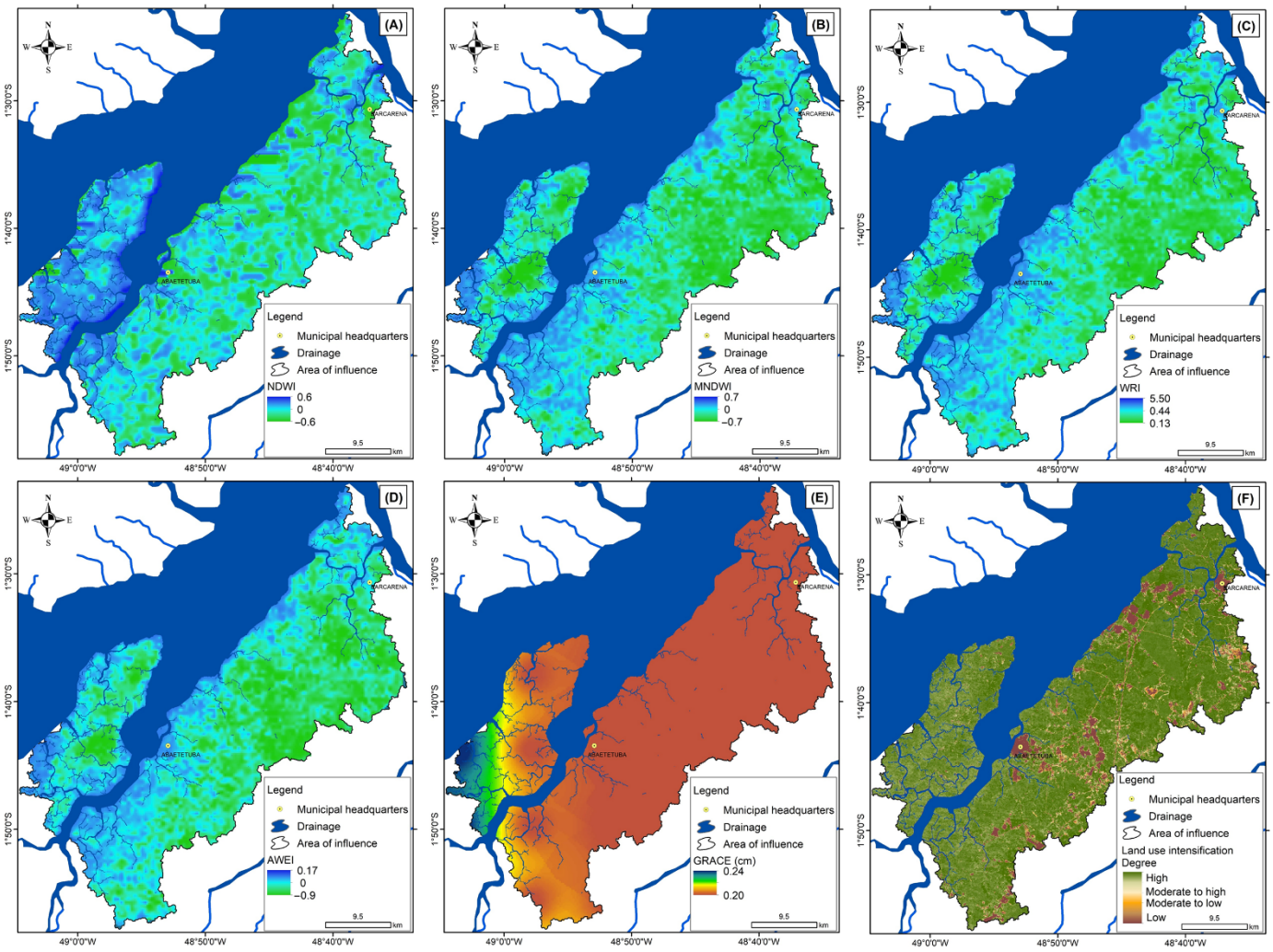


Figure 6. (**A**) Normalized difference water index (NDWI), (**B**) modification of normalized difference water index (MNDWI), (**C**) water ratio index (WRI), (**D**) automated water extraction index (AWEI), (**E**) water mass equivalent (GRACE), and (**F**) degree of land use intensification: land use and presence of wetlands. Correlation sample: NDWI × MNDWI, Pearson = 0.170; NDWI × WRI, Pearson = 0.209; NDWI × AWEI, Pearson = 0.222; MNDWI × WRI, Pearson = 0.287; MNDWI × AWEI, Pearson = 0.936; WRI × AWEI, Pearson = 0.195.

Table 3. Normalized difference water index (NDWI), modified normalized difference water index (MNDWI), automated water extraction index (AWEI), and water ratio index (WRI): distribution around the mean and quartiles.

Statistical Parameters	NDWI	MNDWI	WRI	AWEI
Mean	0.010	−0.397	0.384	−0.549
Median	0.003	−0.412	0.383	−0.585
Standard deviation	0.054	0.128	0.130	0.170
Quartiles (0.25, 0.5, 0.75)	−0.009/0.003/0.022	−0.485/−0.412/−0.327	0.310/0.383/0.467	−0.663/−0.585/−0.467

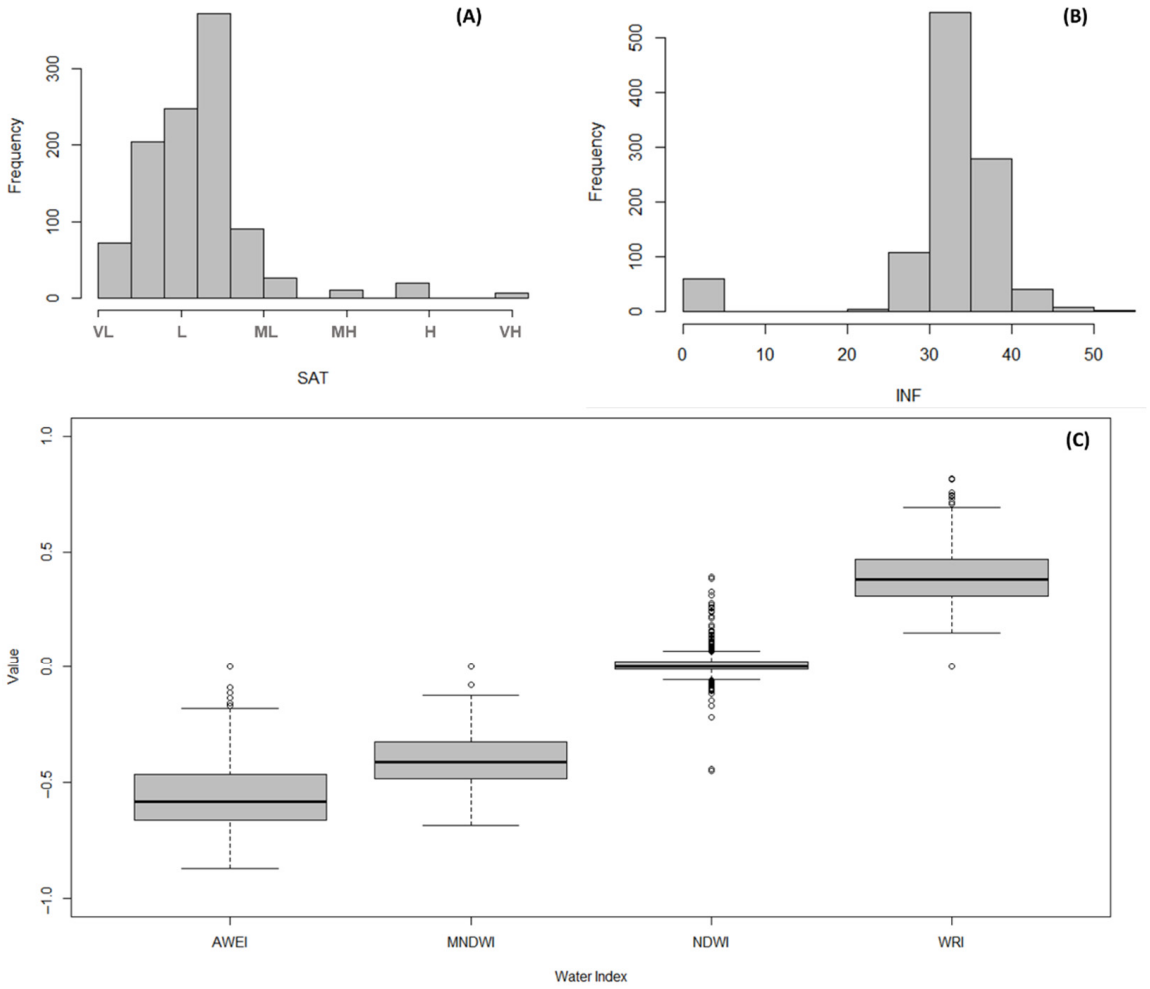


Figure 7. (**A**) Saturation potential in water (SAT). (**B**) Infiltration potential (INF) histogram distribution. (**C**) Normalized difference water index (NDWI), modified normalized difference water index (MNDWI), automated water extraction index (AWEI), and water ratio index (WRI): boxplot distribution.

3.5. Ground-Penetrating Radar (GPR) Application

In a region of Abaetetuba (PA) that experienced two documented mass movement events, in 2014 and 2023, subsurface characterization was carried out using ground-penetrating radar (GPR) (Figures 8 and 9).

The data obtained reveal the presence of reflectors with variations in amplitude and continuity, indicating zones with different dielectric responses associated with material heterogeneity and moisture presence [49,50]. The propagation of electromagnetic waves was limited to a depth of approximately 4 m, consistent with the high electrical conductivity of materials near the surface, influenced by factors such as moisture content, porosity, the presence of clays, and conductive minerals. The estimated propagation speed for the medium was 0.9 m/ns, compatible with saturated soils of fine texture.

In Figure 8A, a significant thickening of the landfill layer is observed, with greater depth compared to the other profiles. Figure 8B shows the radargram obtained near the collapse area recorded in 2023, where irregular reflection patterns are identified, suggesting changes in soil compaction or composition possibly associated with the observed instability (see location in Figure 9C).

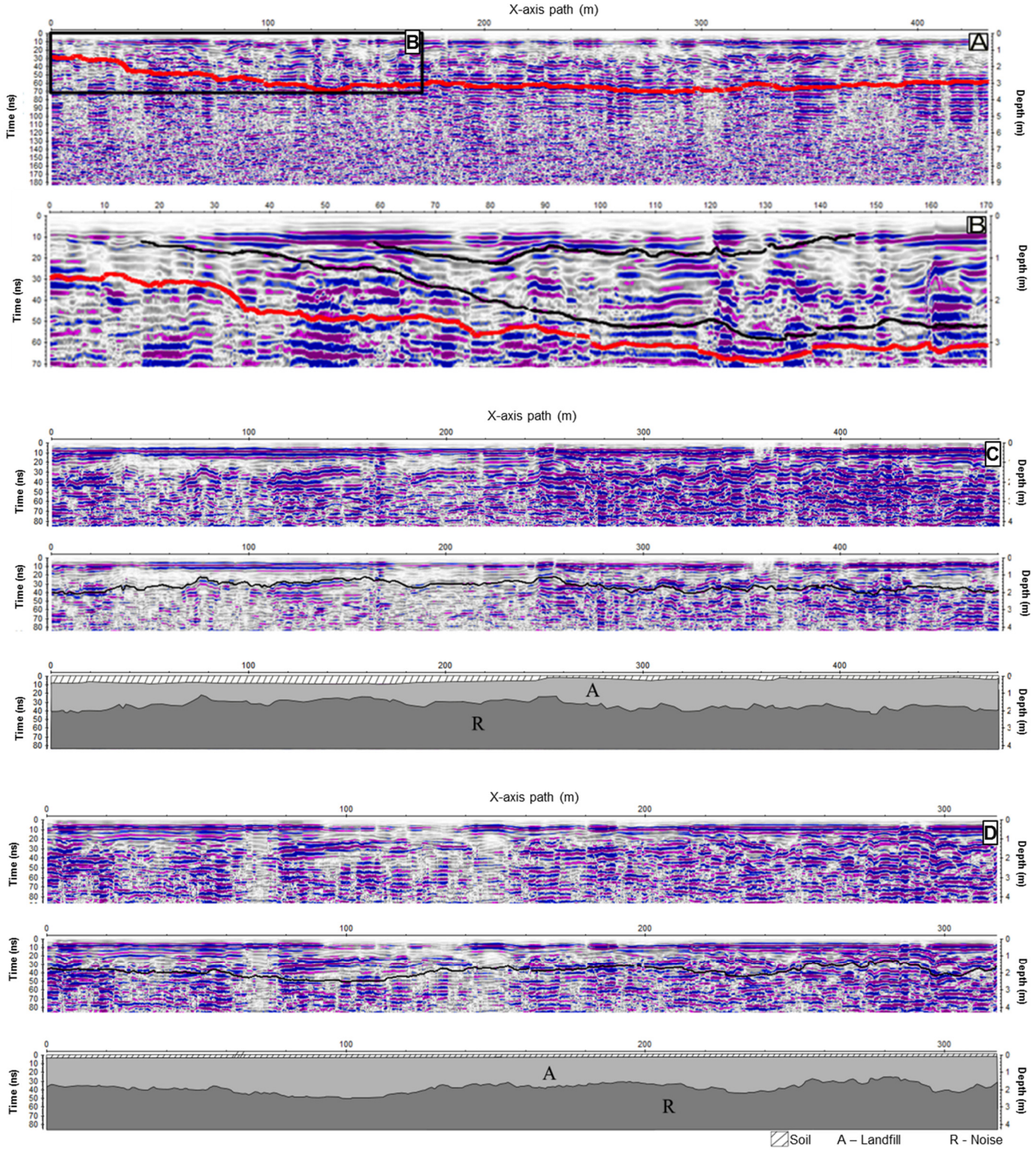


Figure 8. Investigation profiles of an area affected by mass movements in Abaetetuba (PA), obtained by ground-penetrating radar (GPR). (**A**) Profile P12 shows a thicker landfill layer with a depth of over 2 m. (**B**) A detailed view of Profile P12 in the area that collapsed in 2023 shows discontinuous reflections and irregular patterns associated with soil instability. (**C**) Profile P1 which is perpendicular to the estuary and shows variations in the thickness of the landfill layer between 1 and 2 m. (**D**) Profile P8 is transverse to the area of collapse recorded in 2014 and is characterized by a strong electromagnetic signal and a concave feature, which are possibly associated with greater water saturation and the presence of fine sediments.

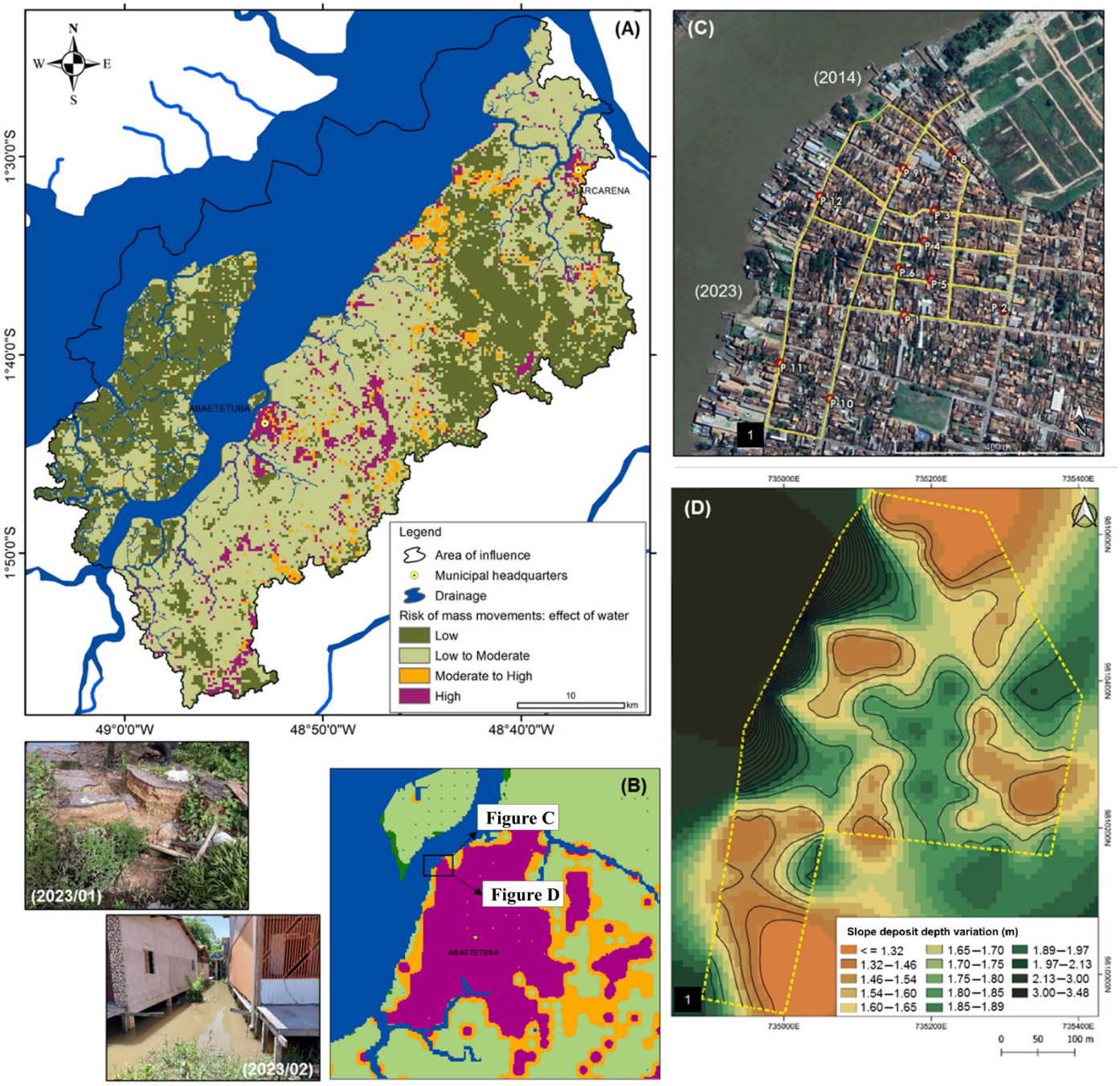


Figure 9. Integrated mass movement information and GPR data in the Abaetetuba urban area (PA). (**A**) Regional map of mass movement due to water action, with highlighting of areas of high susceptibility. (**B**) Local risk map in the central area of Abaetetuba, overlayed with the urban boundaries. Arrows indicate the approximate locations of Figures C and D within the mapped area. (**C**) Satellite image of the study area with the location of the GPR profiles (P1 to P12) and the marking of the affected areas in 2014 and 2023. The solid yellow line represents the streets along which the GPR survey was conducted. (**D**) Digital model of the subsoil obtained by interpolation of the GPR data. It shows variations in thickness and shallow discontinuities in the areas adjacent to the estuary, compatible with zones of instability. The dashed yellow line delineates the boundary of the GPR survey zone, which encompasses the investigated streets. 2023/01 and 2023/02: photographs illustrating the effects of the collapse event that occurred in 2023.

The profile represented in Figure 8C, oriented perpendicularly to the estuary, shows the landfill layer with a thickness variation between 1 and 2 m. Meanwhile, Figure 8D,

obtained in the direction perpendicular to the 2014 collapse site, presents strong reflection associated with high dielectric contrast, highlighting a concave feature consistent with moisture accumulation and sedimentary characteristics of a floodplain. The occurrence of intense and continuous reflections suggests a siliciclastic environment dominated by fine and saturated sediments.

The integrated analysis with risk and land use data shows that the areas affected by the collapses coincide with zones of high susceptibility to mass movements induced by water action (Figure 9A). The interaction between infiltration, water saturation, and anthropogenic alteration of the land, particularly through the replacement of forest cover, indicates that these areas function as wetlands with unstable dynamics. Figure 9D derived from the interpolation of GPR data reveals variations in the thicknesses of surface layers, with shallow contacts and discontinuities in the sectors adjacent to the estuary, especially near the areas affected in 2014 and 2023. These features suggest the presence of unconsolidated substrates of different natures, conditioning the local vulnerability to soil collapse.

4. Discussion

The methodological contribution presented for the study of mass movements associated with soil water saturation aims to assist and complement other studies already developed, with the addition of variables such as precipitation intensity, including duration and cumulative amount [51,52]; remote sensing assessments with high-resolution images and direct extraction of movement indicators [53]; and indicators of geological structure and resulting terrain morphology [9].

In the evaluated region, the research contributes to risk management, where previous studies have already indicated the existing natural vulnerability [16,54] and the need for risk minimization strategies. These include expanding detailed studies, such as those carried out with GPR, in several other points of the city to characterize the subsurface, along with complementary drilling to identify the thicknesses of the existing soil–rock alteration profile [55,56]. Moreover, it is essential to characterize the thicknesses of the landfill material (various grain sizes, including solid waste) present in many parts of the city, which promotes the formation of instability zones.

Wetland areas, such as floodplains and river channels, differ in terms of their geomorphological evolution or morphodynamics. However, they all exhibit repetitive patterns of erosion and sedimentation that are directly affected by variations in water levels and rainfall [57]. Soil erosion and flooding in the Amazon River delta-estuary (ADE) are often associated with various physical and anthropogenic factors. In order to understand the nature and extent of these events, multiple hydrological, meteorological, and geomorphological factors and their patterns must be taken into account. However, insufficient field investigations and the lack of long-term monitoring sites have led to studies combining remote sensing (RS) and Geographic Information Systems (GIS) data with various models and methods to better understand these processes [58].

In this context the use of products from platforms like Google Earth Engine (GEE) also stands out, offering important advantages due to its architecture with updated data, dynamic geospatial processing, and the possibility of internal (within the platform) or external integration with other databases [51]. Remote sensing products associated with advanced technical evaluations, such as machine learning methods, are powerful tools for handling numerous relationships, and they can better understand vulnerability indicators and predict hazard events; furthermore, they can compare the probability of events and produce different models [59].

The integrated mapping using sensors and its association with local surveys with geophysical data proves to be an important strategy for managing potential risk areas. The

applications are diverse, involving the assessment of soil deformation processes, subsidence mechanisms, spatial variability of deformation, and displacement rates [49,50]. Studies related to soil movements need to be conducted frequently according to guidelines based on inventorying, identifying predisposing factors, evaluating them statistically, and proposing predictive models of susceptibility [60].

The occupation of areas bordering rivers is common in the Amazon region, so it is necessary to establish a monitoring routine to identify the growth of cities and the natural and human-induced vulnerabilities associated with the removal of forest cover and the direct exposure of soil to rainwater and rivers [15,16]. Problems in fluvial systems tend to center on efforts to understand how floodplains function at various levels of geomorphological and hydrological complexity. Coupling geophysical approaches with remote sensing methodologies has the potential to address this gap, developing a contextual understanding of environmental forcing conditions, especially in urban areas where non-invasive methods are preferable. These approaches can reduce surveying time and costs while providing detailed insights into subsurface features [61,62].

The ADE is a region where intense natural, social, and economic dynamics are exhibited, with water being strongly involved in food production, human supply, and navigation [10]. Given this, governance actions by the government must seek to reduce the social vulnerability of populations living in risk zones [12] by seeking technological proposals [25,30,43] for preventive and corrective management in the most critical areas. One such area is the sector encompassing the right bank of the ADE, which includes the cities of Barcarena and Abaetetuba.

5. Conclusions

The occupation of marginal areas along rivers in the Amazon region is a traditional practice resulting from the historical settlement marked by rivers serving as an alternative for transportation. Consequently, many cities were established and continue to develop along the banks of watercourses, altering the floodplain or wetland landscape. Landfilling became a common practice, generating a heterogeneous profile that is vulnerable to movement and removal by erosive processes, both due to rainfall and fluvial system action.

The analysis methodology developed aimed to address this scenario with the systematic mapping of water-saturated areas with movement potential. It was shown by the results that the accumulated annual precipitation ranged from 70.07 ± 55.35 mm·month^{-1} to 413.34 ± 127.51 mm·month^{-1}; an accuracy greater than 90% for NDWI, MNDWI, and AWEI was obtained for the same targets by the response similarity across different sensors; and the mass movement concentration in Abaetetuba city was defined by a landfill layer with a thickness variation between 1 and 2 m.

Remote sensing was the alternative to the lack of geological and geotechnical data, while in situ GPR evaluation was proposed as a method to detail a previously observed movement condition to investigate the associated causes. The work was considered successful in performing a mapping process that can be systematically and continuously monitored, and which is also supported by the development of annual water index maps. However, it is recognized that it is necessary to complement this with data from in situ surveys to identify the thickness of the landfill material applied in various areas, as well as specific tests for porosity and permeability of the region's substrate, at least up to the range of 1.5 to 2 m, which proved to be the most dynamic.

Local governments need to invest in remote sensor monitoring and drilling surveys to track the development of mass movement features as well as to understand their relationship with local hydrodynamics, assessing potential groundwater recharge areas that contribute to water circulation in the more subsurface layers. In this way, it would be

possible to respond to the local society, which has already experienced material losses associated with mass movement events and the intensification of erosive processes, leading to soil loss and, consequently, the need for intervention in cities and their growth patterns.

Author Contributions: Conceptualization, A.M.M.d.L., V.G.Q.d.N. and S.S.M.; methodology, A.M.M.d.L., V.G.Q.d.N. and S.S.M.; formal analysis, A.M.M.d.L. and V.G.Q.d.N.; investigation and field work, A.M.M.d.L., V.G.Q.d.N., S.S.M., A.C.S.d.O. and Y.A.d.S.R.; resources, A.M.M.d.L.; writing—original draft preparation, A.M.M.d.L.; writing—review and editing, A.M.M.d.L., S.S.M. and Y.A.d.S.R. All authors have read and agreed to the published version of the manuscript.

Funding: This research was supported by a productivity grant (bolsa produtividade) awarded to the lead author by the National Council for Scientific and Technological Development (CNPq), and by institutional support from the Federal University of Pará (UFPA).

Data Availability Statement: The original contributions presented in this study are included in the article. Further inquiries can be directed to the corresponding author.

Acknowledgments: The authors of this work would like to thank the State of Pará's Civil Defense and the Hydro-environmental Studies and Modeling Laboratory at the Federal University of Pará's Institute of Geosciences.

Conflicts of Interest: The authors declare no conflicts of interest.

References

1. Mansur, A.V.; Brondízio, E.S.; Roy, S.; Hetrick, S.; Vogt, N.D.; Newton, A. An assessment of urban vulnerability in the Amazon Delta and Estuary: A multi-criterion index of flood exposure, socio-economic conditions and infrastructure. *Sustain. Sci.* **2016**, *11*, 625–643. [CrossRef]
2. Ribeiro, R.M.; Amaral, S.; Monteiro, A.M.V.; Dal'Asta, A.P. "Cities in the forest" and "cities of the forest": An environmental Kuznets curve (EKC) spatial approach to analyzing the urbanization–deforestation relationship in a Brazilian Amazon state. *Ecol. Soc.* **2022**, *27*, 2. [CrossRef]
3. Riquetti, N.B.; Beskow, S.; Guo, L.; Mello, C.R. Soil erosion assessment in the Amazon basin in the last 60 years of deforestation. *Environ. Res.* **2023**, *236*, 116846. [CrossRef] [PubMed]
4. Fleischmann, A.S.; Papa, F.; Hamilton, S.K.; Fassoni-Andrade, A.; Wongchuig, S.; Espinoza, J.C.; Paiva, R.C.D.; Melack, J.M.; Fluet-Chouinard, E.; Castello, L.; et al. Increased floodplain inundation in the Amazon since 1980. *Environ. Res. Lett.* **2023**, *18*, 034024. [CrossRef]
5. Staal, A.; Flores, B.M.; Aguiar, A.P.D.; Bosmans, J.H.; Fetzer, I.; Tuinenburg, O.A. Feedback between drought and deforestation in the Amazon. *Environ. Res. Lett.* **2020**, *15*, 044024. [CrossRef]
6. Espinoza, J.C.; Marengo, J.A.; Schongart, J.; Jimenez, J.C. The new historical flood of 2021 in the Amazon River compared to major floods of the 21st century: Atmospheric features in the context of the intensification of floods. *Weather Clim. Extrem.* **2022**, *35*, 100406. [CrossRef]
7. Espinoza, J.C.; Jimenez, J.C.; Marengo, J.A.; Schongart, J.; Ronchail, J.; Lavado-Casimiro, W.; Ribeiro, J.V.M. The new record of drought and warmth in the Amazon in 2023 related to regional and global climatic features. *Sci. Rep.* **2024**, *14*, 8107. [CrossRef]
8. Abuzied, S.M.; Pradhan, B. Hydro-geomorphic assessment of erosion intensity and sediment yield initiated debris-flow hazards at Wadi Dahab Watershed, Egypt. *Georisk* **2021**, *15*, 221–246. [CrossRef]
9. Malka, A. GIS-Based Landslide Susceptibility Modelling in Urbanized Areas: A Case Study of the Tri-City Area of Poland. *GeoHazards* **2022**, *3*, 508–528. [CrossRef]
10. Costa, S.M.F.; Rosa, N.C. O processo de urbanização na Amazônia e suas peculiaridades: Uma análise do delta do rio Amazonas. *Rev. Políticas Públicas Cid.* **2017**, *5*, 81–105.
11. Oliveira, J.A. Tempo e espaço urbano na Amazônia no período da borracha. Scripta Nova. *Rev. Electrónica De Geogr. Y Cienc. Soc.* **2006**, *10*, 218.
12. Ribeiro, R.M.; Ferreira, A.E.D.M.; Cardoso, A.C.D.; Monteiro, A.M.V.; Dal'Asta, A.P.; Carmo, M.B.S.; Amaral, S. A trama urbana amazônica: Proposta metodológica para reconhecimento de um território de possibilidades. *Rev. Bras. De Estud. Urbanos E Reg.* **2024**, *26*, e202433pt. [CrossRef]
13. Cardoso, A.C.D.; Lima, J.J.F.; Ponte, J.P.X.; Ventura, R.D.S.; Rodrigues, R.M. Morfologia urbana das cidades amazônicas: A experiência do Grupo de Pesquisa Cidades na Amazônia da Universidade Federal do Pará. *URBE—Rev. Bras. De Gestão Urbana* **2020**, *12*, e20190275. [CrossRef]

14. Milana, J.P.; Geisler, P. Forensic Geology Applied to Decipher the Landslide Dam Collapse and Outburst Flood of the Santa Cruz River, San Juan, Argentina. *GeoHazards* **2022**, *3*, 252–276. [CrossRef]
15. Brondizio, E.S.; Vogt, N.; Mansur, A.V.; Anthony, E.J.; Costa, S.M.F.; Hetrick, S. A conceptual framework for analyzing deltas as coupled social-ecological systems: An example from the Amazon River Delta. *Sustain. Sci.* **2016**, *11*, 591–609. [CrossRef]
16. Rocha, Y.A.D.S.; Lima, A.M.M.D.; Silva, C.M.S.E.; Franco, V.D.S.; Raiol, L.L.; Oliveira, I.S.D.; Dias, M.L.M.; Beltrão Júnior, P.R.E. Hydro-meteorological dynamics of rainfall erosivity risk in the Amazon River Delta-Estuary. *J. Water Clim. Change* **2025**, *16*, 1673–1694. [CrossRef]
17. Edmonds, D.A.; Caldwell, R.L.; Brondizio, E.S.; Siani, S.M.O. Coastal flooding will disproportionately impact people on river deltas. *Nat. Commun.* **2020**, *11*, 4741. [CrossRef] [PubMed]
18. Pereira, L.E.; Amorim, G.; Grigio, A.M.; Paranhos Filho, A.C. Análise Comparativa entre Métodos de Índice de Água por Diferença Normalizada (NDWI) em Área Úmida Continental. *Anuário Do Inst. De Geociências* **2018**, *41*, 654–662. [CrossRef]
19. Liu, S.; Wu, Y.; Zhang, G.; Lin, N.; Liu, Z. Comparing Water Indices for Landsat Data for Automated Surface Water Body Extraction under Complex Ground Background: A Case Study in Jilin Province. *Remote Sens.* **2023**, *15*, 1678. [CrossRef]
20. Land Processes Distributed Active Archive Center (LPDAAC); U.S. Geological Survey (USGS); Earth Observing System Data and Information System (EOSDIS); National Aeronautics and Space Administration (NASA). Google Earth Product: MOD09A1.061 Terra Surface Reflectance 8-Day Global: Ee.ImageCollection("MODIS/061/MOD09A1"); MODIS Combined 16-Day NDWI: Ee.ImageCollection("MODIS/MCD43A4_006_NDWI"). 2024. Available online: https://lpdaac.usgs.gov/data/data-citations-and-guidelines/ (accessed on 29 January 2025).
21. Landerer, F.W.; Swenson, S.C. Accuracy of scaled GRACE terrestrial water storage estimates. *Water Resour. Res.* **2012**, *48*, W04531. Google Earth product: GRACE Monthly Mass Grids Release 06 Version 04—Land: Ee.ImageCollection ("NASA/GRACE/MASS_GRIDS_V04LAND"). [CrossRef]
22. Farr, T.G.; Rosen, P.A.; Caro, E.; Crippen, R.; Duren, R.; Hensley, S.; Kobrick, M.; Paller, M.; Rodriguez, E.; Roth, L.; et al. The shuttle radar topography mission. *Rev. Geophys.* **2007**, *45*, RG2004. Google Earth product: NASA SRTM Digital Elevation 30m: Ee.Image("USGS/SRTMGL1_003"). [CrossRef]
23. Lehner, B.; Verdin, K.; Jarvis, A. New global hydrography derived from spaceborne elevation data. *Eos Trans.* **2008**, *89*, 93–94. Google Earth product: HydroSHEDS Void-Filled DEM: Ee.Image("WWF/HydroSHEDS/03VFDEM"). [CrossRef]
24. Hengl, T.; Gupta, S. Soil water content (volumetric%) for 33kPa and 1500kPa suctions predicted at 6 standard depths (0, 10, 30, 60, 100 and 200 cm) at 250 m resolution (Version v01). *Zenodo* **2019**. Google Earth product: OpenLandMap Soil Water Content (Field Capacity): Ee.Image("OpenLandMap/SOL/SOL_WATERCONTENT-33KPA_USDA-4B1C_M/v01"). [CrossRef]
25. Gupta, S.; Papritz, A.; Lehmann, P.; Hengl, T.; Bonetti, S.; Or, D. Global Mapping of Soil Water Characteristics Parameters-Fusing Curated Data with Machine Learning and Environmental Covariates. *Remote Sens.* **2022**, *14*, 1947. [CrossRef]
26. Hansen, M.C.; Potapov, P.V.; Moore, R.; Hancher, M.; Turubanova, S.A.; Tyukavina, A.; Thau, D.; Stehman, S.V.; Goetz, S.J.; Loveland, T.R.; et al. High-resolution global maps of 21st-century forest cover change. *Science* **2013**, *342*, 850–853. Google Earth product: Hansen/UMD/Google/USGS/NASA: Ee.Image("UMD/hansen/global_forest_change_2023_v1_11"). [CrossRef]
27. SGB. *Estimativa de água disponível nos solos do Brasil*; Catálogo PRONASOLOS, Escala: 1:500.000; Serviço Geológico do Brasil—SGB: Rio de Janeiro, Brazil, 2024. Available online: https://geosgb.sgb.gov.br/geosgb/pronasolos.html (accessed on 20 January 2025).
28. Avaliação, Predição e Mapeamento de Água Disponível em Solos do Brasil. *Boletim de Pesquisa e Desenvolvimento*; Embrapa Solos: Rio de Janeiro, Brazil, 2022; p. 146.
29. Brasil. Agência Nacional de Águas e Saneamento Básico—ANA. HidroWeb: Sistema de Informações Hidrológicas. 2024. Available online: https://www.snirh.gov.br/hidroweb (accessed on 14 January 2025).
30. Li, Q.; Lu, L.; Wang, C.; Li, Y.; Sui, Y.; Guo, H. MODIS-derived spatiotemporal changes of major lake surface areas in arid Xinjiang, China, 2000–2014. *Water* **2015**, *7*, 5731–5751. [CrossRef]
31. Laonamsai, J.; Julphunthong, P.; Saprathet, T.; Kimmany, B.; Ganchanasuragit, T.; Chomcheawchan, P.; Tomun, N. Utilizing NDWI, MNDWI, SAVI, WRI, and AWEI for Estimating Erosion and Deposition in Ping River in Thailand. *Hydrology* **2023**, *10*, 70. [CrossRef]
32. Rocha, A.D.; Vulova, S.; Meier, F.; Förster, M.; Kleinschmit, B. Mapping evapotranspirative and radiative cooling services in an urban environment. *Sustain. Cities Soc.* **2022**, *85*, 104051. [CrossRef]
33. Loizos, A.; Plati, C. Accuracy of pavement thickness estimation using different ground penetrating radar analysis approaches. *NDT E Int.* **2007**, *40*, 147–157. [CrossRef]
34. Annan, A.P. Electromagnetic Principles of Ground Penetrating Radar. In *Ground Penetrating Radar: Theory and Applications*; Jol, H.M., Ed.; Elsevier: Amsterdam, The Netherlands, 2009.
35. Yoon, J.H.; Zeng, N. An Atlantic influence on Amazon rainfall. *Clim. Dyn.* **2010**, *34*, 249–264. [CrossRef]
36. Limberger, L.; Silva, M.E.S. Precipitação na bacia amazônica e sua associação à variabilidade da temperatura da superfície dos oceanos Pacífico e Atlântico: Uma revisão. *GEOUSP: Espaço E Tempo* **2016**, *20*, 657–675. [CrossRef]
37. Liu, Y.; Cai, W.; Zhang, Y.; Lin, X.; Li, Z. Near-term projection of Amazon rainfall dominated by phase transition of the Interdecadal Pacific Oscillation. *Clim. Atmos. Sci.* **2024**, *7*, 46. [CrossRef]

38. João, X.S.J.; Teixeira, S.G.; Fonseca, D.D.F. *Geodiversidade do Estado do Pará*; CPRM: Belém, Brazil, 2013; p. 256.
39. Folha, S.A. *22 Belém. Programa Geologia do Brasil—Cartografia Hidrogeológica*; Carta Hidrogeológica, Escala 1:1.000.000; Serviço Geológico do Brasil (SGB/CPRM): Rio de Janeiro, Brazil, 2016.
40. El-Robrini, M.; Silva, P.V.; Magno, C.; Rodrigues, M.V. Morfodinâmica e transporte de sedimentos em praias amazônicas de meso-marés: O caso da Vila do Conde (Barcarena/Pará). *Cad. De Geogr.* **2023**, *33*, 1300–1328. [CrossRef]
41. Huang, J.; Hartemink, A.E. Soil and environmental issues in sandy soils. *Earth-Sci. Rev.* **2020**, *208*, 103295. [CrossRef]
42. Bronswijk, J.J.B. Modeling of water balance, cracking and subsidence of clay soils. *J. Hydrol.* **1988**, *97*, 199–212. [CrossRef]
43. Coyle, C.; Creamer, R.E.; Schulte, R.P.; O'Sullivan, L.; Jordan, P. A functional land management conceptual framework under soil drainage and land use scenarios. *Environ. Sci. Policy* **2016**, *56*, 39–48. [CrossRef]
44. Javed, A.; Cheng, Q.; Peng, H.; Altan, O.; Li, Y.; Ara, I.; Huq, E.; Ali, Y.; Saleem, N. Review of spectral indices for urban remote sensing. *Photogramm. Eng. Remote Sens.* **2021**, *87*, 513–524. [CrossRef]
45. Ma, S.; Zhou, Y.; Gowda, P.H.; Dong, J.; Zhang, G.; Kakani, V.G.; Wagle, P.; Chen, L.; Flynn, C.; Jiang, W. Application of the water-related spectral reflectance indices: A review. *Ecol. Indic.* **2019**, *98*, 68–79. [CrossRef]
46. Zhao, C.; Wei, H.; Feyisa, G.L.; Castro Tayer, T.; Ma, G.; Wu, H.; Pan, Y. Evaluating spectral indices for water extraction: Limitations and contextual usage recommendations. *Int. J. Appl. Earth Obs. Geoinf.* **2025**, *139*, 104510. [CrossRef]
47. Zhou, Y.; Dong, J.; Xiao, X.; Xiao, T.; Yang, Z.; Zhao, G.; Zou, Z.; Qin, Y. Open surface water mapping algorithms: A comparison of water-related spectral indices and sensors. *Water* **2017**, *9*, 256. [CrossRef]
48. Gümüş, M.G. Performance Analysis of Water Extraction Indices with Geospatial and Statistical Techniques Using Google Earth Engine Platform: A Case Study of Ramsar Wetlands in Türkiye. *J. Indian Soc. Remote Sens.* **2025**, *53*, 2697–2721. [CrossRef]
49. Sevil, J.; Gutiérrez, F.; Carnicer, C.; Carbonel, D.; Desir, G.; García-Arnay, Á.; Guerrero, J. Characterizing and monitoring a high-risk sinkhole in an urban area underlain by salt through non-invasive methods: Detailed mapping, high-precision leveling and GPR. *Eng. Geol.* **2020**, *272*, 105641. [CrossRef]
50. Lago, A.L.; Borges, W.R.; Barros, J.S.; Sousa Amaral, E. GPR application for the characterization of sinkholes in Teresina, Brazil. *Environ. Earth Sci.* **2022**, *81*, 132. [CrossRef]
51. Scheip, C.M.; Wegmann, K.W. HazMapper: A global open-source natural hazard mapping application in Google Earth Engine. *Nat. Hazards Earth Syst. Sci. Discuss.* **2020**, *21*, 1495–1511. [CrossRef]
52. Chen, C.W.; Hung, C.; Lin, G.W.; Liou, J.J.; Lin, S.Y.; Li, H.C.; Chen, Y.M.; Chen, H. Preliminary establishment of a mass movement warning system for Taiwan using the soil water index. *Landslides* **2022**, *19*, 1779–1789. [CrossRef]
53. Assis, L.E.; Marques, E.A.G.; Lima, C.A.; Menezes, S.J.M.C.; Roque, L.A. Mapping of Geological-Geotechnical Risk of Mass Movement in an Urban Area in Rio Piracicaba, MG, Brazil. *Soils Rocks* **2020**, *43*, 57–70. [CrossRef]
54. Bandeira, I.C.N.; Adamy, A.; Andretta, E.R.; Costa da Conceição, R.A.; Andrade, M.M.N. Terras caídas: Fluvial erosion or distinct phenomenon in the Amazon? *Environ. Earth Sci.* **2018**, *77*, 222. [CrossRef]
55. Mendes, A.; Galvão, P.; Sousa, J.; Silva, I.; Carneiro, R.N. Relations of the groundwater quality and disorderly occupation in an Amazon low-income neighborhood developed over a former dump area, Santarém/PA, Brazil. *Environ. Dev. Sustain.* **2019**, *21*, 353–368. [CrossRef]
56. Di Prinzio, M.; Bittelli, M.; Castellarin, A.; Pisa, P.R. Application of GPR to the monitoring of river embankments. *J. Appl. Geophys.* **2010**, *71*, 53–61. [CrossRef]
57. Wierzbicki, G.; Ostrowski, P.; Falkowski, T. Applying floodplain geomorphology to flood management (The Lower Vistula River upstream from Plock, Poland). *Open Geosci.* **2020**, *12*, 1003–1016. [CrossRef]
58. Ashfaq, S.; Tufail, M.; Niaz, A.; Muhammad, S.; Alzahrani, H.; Tariq, A. Flood susceptibility assessment and mapping using GIS-based analytical hierarchy process and frequency ratio models. *Glob. Planet. Change* **2025**, *251*, 104831. [CrossRef]
59. Xiao, T.; Zhang, L.M. Data-driven landslide forecasting: Methods, data completeness, and real-time warning. *Eng. Geol.* **2023**, *317*, 107068. [CrossRef]
60. Zêzere, J.L.; Pereira, S.; Melo, R.; Oliveira, S.C.; Garcia, R.A. Mapping landslide susceptibility using data-driven methods. *Sci. Total Environ.* **2017**, *589*, 250–267. [CrossRef]
61. Famiglietti, N.A.; Miele, P.; Massa, B.; Memmolo, A.; Moschillo, R.; Zarrilli, L.; Vicari, A. Ground Penetrating Radar (GPR) Investigations in Urban Areas Affected by Gravity-Driven Deformations. *Geosciences* **2024**, *14*, 222. [CrossRef]
62. Schwendel, A.C.; Milan, D.J.; Pope, R.J.; Williams, R.; Thompson, W. Using geophysical subsurface data for the reconstruction of valley-scale spatio-temporal floodplain evolution: Implications for upland river restoration. *Geomorphology* **2024**, *466*, 109459. [CrossRef]

Disclaimer/Publisher's Note: The statements, opinions and data contained in all publications are solely those of the individual author(s) and contributor(s) and not of MDPI and/or the editor(s). MDPI and/or the editor(s) disclaim responsibility for any injury to people or property resulting from any ideas, methods, instructions or products referred to in the content.